Chemical Engineering Science 201 (2019) 201–211

Contents lists available at ScienceDirect

Chemical Engineering Science

journal homepage: www.elsevier.com/locate/ces

LBM study of aggregation of monosized spherical particles in homogeneous isotropic turbulence

Guichao Wang [a], Dongdong Wan [b], Cheng Peng [c], Ke Liu [a], Lian-Ping Wang [c,d,*]

[a] SUSTech Academy for Advanced Interdisciplinary Studies, Southern University of Science and Technology, Shenzhen 518055, PR China
[b] Key Laboratory of High-efficiency and Clean Mechanical Manufacture, School of Mechanical Engineering, Shandong University, Jinan 250061, PR China
[c] Department of Mechanical Engineering, 126 Spencer Laboratory, University of Delaware, Newark, DE 19716-3140, USA
[d] Department of Mechanics and Aerospace Engineering, Southern University of Science and Technology, Shenzhen 518055, PR China

HIGHLIGHTS

- A particle-resolved DNS simulation of aggregation in turbulence is conducted.
- The effect of aggregating particles on turbulence is evaluated.
- The effect of particle volume concentration on aggregation is assessed.

GRAPHICAL ABSTRACT

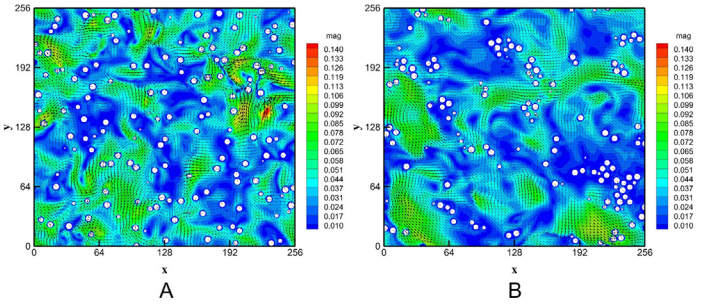

ARTICLE INFO

Article history:
Received 2 December 2018
Received in revised form 1 March 2019
Accepted 4 March 2019
Available online 6 March 2019

Keywords:
Lattice Boltzmann method
Mono-sized spherical particles
Aggregation
Turbulence

ABSTRACT

Direct numerical simulations of an aggregation system composed of monosized spherical particles in homogeneous isotropic turbulence have been performed using Lattice Boltzmann method (LBM). The effects of hydrodynamics on the aggregation process were considered by directly resolving the disturbance flows around finite-size solid particles using an interpolated bounce-back scheme. A nonuniform time-dependent large-scale stochastic forcing scheme was implemented within the mesoscopic multiple-relaxation-time LBM approach to maintain turbulence intensity at targeted levels. To simulate particle interactions, the non-contact surface force and the contact force were taken into account using the Derjaguin-Landau-Verwey-Overbeek (DLVO) theory and the soft-sphere model, respectively. This interface-resolved direct numerical simulation (IR-DNS) combined with the well-known DLVO theory was employed to obtain an insight into the aggregation process of micron-size particles. Specifically, the model was used to study the effects of solid volume fraction on aggregate growth. Aggregates of larger sizes formed in local regions of higher concentration of particles due to higher encountering probability between particles. The effects of aggregating particles of different volume fractions on the statistically stationary homogeneous isotropic turbulent flow were investigated. It was found that the presence of particles attenuated the turbulent kinetic energy at large scales and augmented the kinetic energy at the small scales. This effect is more apparent with increasing volume concentration of particles.

© 2019 Elsevier Ltd. All rights reserved.

* Corresponding author at: Department of Mechanical Engineering, 126 Spencer Laboratory, University of Delaware, Newark, DE 19716-3140, USA.
E-mail address: wanglp@sustc.edu.cn (L.-P. Wang).

https://doi.org/10.1016/j.ces.2019.03.004
0009-2509/© 2019 Elsevier Ltd. All rights reserved.

1. Introduction

Aggregation of small particles is commonly encountered in many industrial processes including water treatment, mineral beneficiation and dewatering, and biological separation processes (Bratby, 2006; Vandamme et al., 2013; Wang et al., 2014a; Wang et al., 2018a). The effective management and disposal of suspensions containing colloidal particulate matters are important from both environmental and water recovery perspectives. Particle aggregation refers to formation of assemblages in a suspension and during this process particles stick to each other forming larger-size clusters or aggregates. The efficiency of such processes often depends on the rate and extent of aggregation and subsequently the size and structure of the aggregates formed in the suspension. An optimum flow environment can be achieved by eliminating insufficient mixing and by generating a flow field where aggregates can form to their optimum size and strength simultaneously. Particle-fluid and particle-particle interactions play an important role in aggregation process. It is desirable to understand the formation and dynamics of aggregation of suspensions composed of different particle volume fractions in a turbulent field.

Nevertheless, few studies have incorporated hydrodynamic models to directly simulate the formation and settling of particle aggregates in aggregation processes. Due to the difficulties in modeling fluid–particle interactions and structures of particle aggregates, the effect of turbulence on aggregation process is still a poorly understood phenomenon (Thomas et al., 1999). With development in computational methods and increasing computational power, the use of computational fluid dynamics (CFD) and discrete element model (DEM) for detailed simulations of aggregation is being developed extensively. Bridgeman et al. (2009) presented a critical review of current approaches using CFD to model the inter-related hydrodynamic, physical and chemical processes involved in the aggregation. The turbulent flow is usually modelled by the two-equation models and such an approach, while computationally efficient, has been found to produce often inaccurate results compared to experimental data. CFD has been developed as a tool for simulating the operation of aggregation tanks with the purpose of the optimization of the design and operation of aggregation (Karpinska and Bridgeman, 2016; Samaras et al., 2010; Vadasarukkai et al., 2011; Wang et al., 2018b). Few researchers have studied particle tracking using a Lagrangian model. Peng et al. (2010; 2012a; 2012b) used the DEM method to study the aggregation of suspended nanoparticles and the influence of particle size distribution and aggregate structure on suspension shear yield stress.

With the rapid development of Lattice Boltzmann method (LBM), this method can be applied to explore the mechanisms of aggregation processes. The LBM has developed into a mesoscopic simulation tool for the computation of incompressible flow, giving essentially second-order accuracy in space and time (Chen and Doolen, 1998). In the simulation of fully resolved flow around particles, Ladd (1994a, 1944b) introduced a particularly efficient and simple way to enforce the no-slip boundary condition on a sphere in the LB method. According to the no-slip boundary condition, the fluid velocity relative to the particle surface velocity vanishes at the surface of the solid spheres. By identifying the boundary nodes as the points halfway between any pair of neighboring lattice sites where one is located inside the sphere and the other one is outside the sphere, the lattice particle distribution bounces back at the boundary node resulting in a zero-average velocity at the boundary node. In this way, the LBM does not require a closure relationship for the particle–fluid interaction force, as the force can be computed directly through the net momentum exchange from all bounce-back operations.

The implementations of the LBM for simulations of suspended particles (Ladd and Verberg, 2001; Nguyen and Ladd, 2002; Zhou et al., 2017) and many particle systems in sedimentation (Nguyen and Ladd, 2005) and Couette systems (Kromkamp et al., 2006), have proved to be simple and robust for lower–Reynolds number flows. Zhang and Zhang (2008) used LBM to describe the complicated fractal floc settling behavior. Zhang and Zhang (2011) used the LBM to study the aggregation processes of cohesive sediment due to differential settling. Zhang et al. (2013) further extended this method in the study of aggregation of cohesive sediment induced by turbulence. Turbulent shear was shown to be a significant factor on the floc size, floc settling velocity, and collision frequency. Ernst et al. (2013) used the LBM to study the agglomeration of freely moving spherical particles. Particles were considered to always stick together and form aggregates once two particles touched each other. Derksen (2012) used the LBM to study the aggregation of monosized spherical particles in homogeneous isotropic turbulence. Turbulence interacts with the aggregation process in two ways: on the one hand it promotes collisions that potentially lead to aggregation events, on the other hand the local shear-induced hydrodynamic forces from turbulent flow can lead to the breakage of aggregates. The aggregate size distributions were found dependent on both the strength of particle–particle interactions and the intensity of the turbulence. Turbulent fluctuations of the hydrodynamic stress along the aggregate trajectory were found to play a key role in the breakage of aggregates (Babler et al., 2012). The breakup rates were found to be substantially different in the different flow configurations, highlighting the importance of flow inhomogeneity and turbulent fluctuations (Babler et al., 2015). Three-dimensional particle tracking velocimetry was also used to measure aggregate trajectories and the full velocity gradient tensor along their pathlines (Saha et al., 2015). Drag stress was found to play an important role at the location of breakage compared to shear stress and normal stress at the location of breakage.

Resolved simulations of multiple particles in isotropic turbulence are developing using different methods (Chouippe and Uhlmann, 2015; Vreman, 2016). In the current work, a LBM model has been developed to study the aggregation of monosized spherical particles has been developed and the simulation results of the aggregation hydrodynamics, fluid–particle interactions, and particle–particle collision behaviour will be reported. Nevertheless, the same methodology developed in our group has been successfully applied to investigate the modulation of turbulence by finite-size solid particles (Wang et al., 2014b). This methodology is extended to study the aggregation of monosized spherical particles in homogeneous isotropic turbulence. The statistical properties of a group of particles in the forced turbulent flow and the modulations of both the mean flow velocity and turbulent intensity by solid particles are analyzed to probe multiscale physics in aggregation processes.

2. Problem setup and numerical method

2.1. Problem description of an aggregation system

In order to keep the computations affordable, the simulation area was restricted to a "box" (referred to as the reconstructed domain). The aggregation of spherical monodisperse particles were simulated in a cubic domain defined as fully-periodic boundary conditions in all dimensions. It is assumed that the same aggregation behaviour in the simulated domain could be repeated within the whole system and the aggregation occurred far from the edges where the boundary effect was negligible.

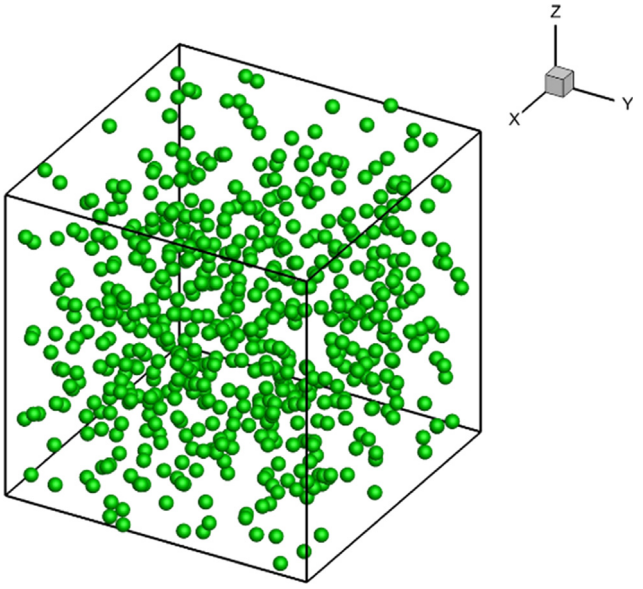

Fig. 1. Sketch of an aggregation system with particles at a volume fraction of 1% uniformly distributed in the cubic domain.

As shown in Fig. 1, a number of monodisperse spherical particles are inserted into a reconstructed domain. Simulations of the aggregation process were performed in the reconstructed domain (32dp × 32dp × 32dp), for five different average particle volume fractions (φ_p). The parameters of the background flow are given in Table 1. The analysis of the effect of the particle volume fraction on the aggregation process was performed on five different particle volume fractions in the range from 1 to 9%.

2.2. The lattice Boltzmann method

The model was built based on the lattice Boltzmann method (D3Q19, three-dimensional nineteen discrete velocities) incorporating a sharp-interface treatment of no-slip condition on particle surfaces. LBM solves in a few selected discrete velocities the evolution of the molecular distribution functions from which the hydrodynamic quantities, such as pressure and velocity fields are directly obtained by taking moments. The multiple-relaxation time (MRT) collision model was selected for its better numerical stability over the single-relaxation time (SRT) model. Bounce-back schemes were used to treat no-slip boundary conditions with minimal numerical dissipation. In this study, an interpolated bounce-back scheme designed by Lallemand and Luo (2003) was adopted to treat the interaction of the fluid with moving solid surfaces as the default scheme for the no-slip boundary condition.

The studied domain is discretized into a number of lattice nodes residing on a uniform cubic grid. In the LBM, fluid lattice particles of unique velocities move from each node to its neighbors according to prescribed rules. There are 19 lattice velocities labelled from 0 to 18 in D3Q19 lattice grid. LBM solves the evolution of mesoscopic particle distribution functions as

$$f_i\left(\vec{x}+\vec{e}_i\delta_t, t+\delta_t\right)-f_i\left(\vec{x},t\right) = -\boldsymbol{M}^{-1}\boldsymbol{S}\left[\boldsymbol{m}\left(\vec{x},t\right)-\boldsymbol{m}^{(eq)}\left(\vec{x},t\right)\right]+Q \quad (1)$$

where f_i is the vector of distribution functions, $\vec{e}_i$ are the selected discrete velocities, $\vec{x}$ and t are the spatial and time coordinate, respectively. δ_t is the lattice time step, M is the transform matrix that relates the distribution functions vector f_i to a moments vector m with the same length. $\boldsymbol{m}^{(eq)}$ is the equilibrium part of m. S is diagonal matrix of relaxation parameters. The dx is 1 in lattice units. The term Q denotes a forcing field in the mesoscopic space to produce a desired non-uniform, time-dependent, large-scale physical space forcing field F(x,t). We apply the well-known stochastic forcing scheme of Eswaran and Pope (1988b) to drive the turbulent flow for the advantage of predictable energy input. The average net rate of energy input through the forcing scheme, which is also equal to the average viscous dissipation rate, can be expressed empirically as

$$\text{rate of energy input} = \frac{4N_f\sigma_f^2T_f}{1+T_f\left(\sigma_f^2T_fN_fk_0^2\right)^{1/3}\Big/\beta} \quad (2)$$

where the number of forced modes is $N_f = 80$ and the lowest wavenumber in spectral units is $k_0 = 1$. β is a fitting parameter. Based on their lower resolution simulations, Eswaran and Pope (1988b) found that $\beta \approx 0.8$. In this type of forcing, the flow could be initialized from any random field of $\mathbf{U}(\mathbf{x}, t)$. This stochastic method forces the Fourier modes of $|\mathbf{k}| < 2.5$ by amplifying the velocity vector in Fourier space to achieve a predefined energy spectrum, for the two low wave number band. The preset values of energy are obtained so that their ratio satisfies $k^{-5/3}$ energy spectrum, after accounting for the number of modes forced in each shell volume. More information about the large-scale forcing, MPI implementation as well as definitions of the moments, and their corresponding equilibria in the present D3Q19 MRT-LBM model can be found in the references (Gao et al., 2013; Wang et al., 2014b). Here, this information will not be repeated.

2.3. Suspended particles

After the hydrodynamic force/torque, the lubrication force, the collision force and van der Waals force acting on the particle are calculated. The translational and rotational velocities of a single particle within a suspension are based on Newton's equation of motion. The particle translational velocity V, position Y, angular velocity Ω and displacement Θ are updated as

$$\begin{aligned} V^{t+\delta t} &= V^t+\tfrac{1}{M_p}\left(\tfrac{F^{t+\delta t/2}+F^{t-\delta t/2}}{2}+F_{lub}^t+F_{VD}^t+F_s^t\right)\delta t,\\ Y^{t+\delta t} &= Y^t+\tfrac{1}{2}\left(V^{t+\delta t}+V^t\right)\delta t,\\ \Omega^{t+\delta t} &= \Omega^t+\tfrac{1}{I_p}\left(\tfrac{\Gamma^{t+\delta t/2}+\Gamma^{t-\delta t/2}}{2}\right)\delta t,\\ \Theta^{t+\delta t} &= \Theta^t+\tfrac{1}{2}\left(\Omega^{t+\delta t}+\Omega^t\right)\delta t, \end{aligned} \quad (3)$$

where Mp and Ip are the mass and moment of inertia of the particle. It should be noted that the hydrodynamic force F and torque Γ are expressed at half time. Since the momentum exchange actually happens somewhere between t to t + δt during the streaming process. This feature allows the natural application of trapezoidal rule in the update of the particle velocity and angular velocity. The lubrication force, however, is calculated based on the initial particle position and velocity at t. The van der Waals force is calculated based on the surface properties of particles, which is explained in

Table 1
Calculation parameters and simulated statistics in forced single-phase and particle-laden turbulent flows.

Grid resolution N^3	256^3
Viscosity ν	7.844×10^{-3}
dp/dx	8
Particle volume fraction	1%, 3%, 5%, 7%, 9%
dp/η	8.8
ρ_p/ρ_f	5
Restitution coefficient	0.1
Hamaker's constant	1.5×10^{-20} J

the next section. Finally, the particle position and angular displacement are proceeded to t + δt using a simple trapezoidal rule.

2.4. The force models

- Lubrication force model and soft-sphere collision model

When two particles are in close proximity with a separation of the order of or less than the lattice spacing, the hydrodynamic interactions between them could not be properly resolved in the LB simulations, Therefore, lubrication forces are explicitly imposed on the particles and the lubrication force model in Brändle de Motta et al. (2013) was used to handle the particle-particle interactions. The lubrication force was applied with the coefficients $\varepsilon_0 = 0.125$ for particle-particle interactions. The piece-wise lubrication force model as is shown in Fig. 2 was implemented, which is written as:

$$\boldsymbol{F}_{lub} = 6\pi\mu R_p \boldsymbol{u}_n[\lambda(\varepsilon) - \lambda(\varepsilon_{al})] \tag{4}$$

where λ is the asymptotic function of ε, ε_{al} is the threshold distance below which the lubrication force is turned on. The choice of ε_{al} may depend on the specific numerical method one uses. Typically, when the gap distance between two solid objects is smaller than one grid spacing, the flow inside the gap is usually unresolved and the lubrication force model has to play a role. λ for particle-particle interactions, to the order of O(ε) is:

$$\lambda(\varepsilon) = \frac{1}{2\varepsilon} - \frac{9}{20}\ln\varepsilon - \frac{3}{56}\varepsilon\ln\varepsilon + 1.346 + O(\varepsilon) \tag{5}$$

A soft-sphere collision model in (Brändle de Motta et al., 2013) was employed to prevent the two solid objects in physical contact from generating nonphysical overlapping. This model is essentially a spring-dashpot system, which reads as

$$\boldsymbol{F}_s = (-k_n\zeta - \beta_n u_n)\boldsymbol{n} \tag{6}$$

where

$$k_n = \frac{m_e\left[\pi^2 + (\ln e_d)^2\right]}{(N_c\delta_t)^2},\ \beta_n = -\frac{2m_e(\ln e_d)}{N_c\delta_t},\ m_e = \frac{1}{\left(\frac{1}{m_i} + \frac{1}{m_j}\right)}, \tag{7}$$

are the stiffness of the spring and the damping coefficient of the dashpot, *me* is the effective mass, respectively. *ed* is the collision coefficient of restitution, *Ncδt* is the collision period. Ideally, *Nc* should be as small as possible to mimic the ephemeral collisions period in reality. On the other hand, *Nc* must also be sufficient large so the collision process is well resolved. Brändle de Motta et al. (2013) suggested *Nc* should be made small but no smaller than 8. The collision restitution coefficient is given as 0.1 following the setup used in the work by Sun et al. (2018).

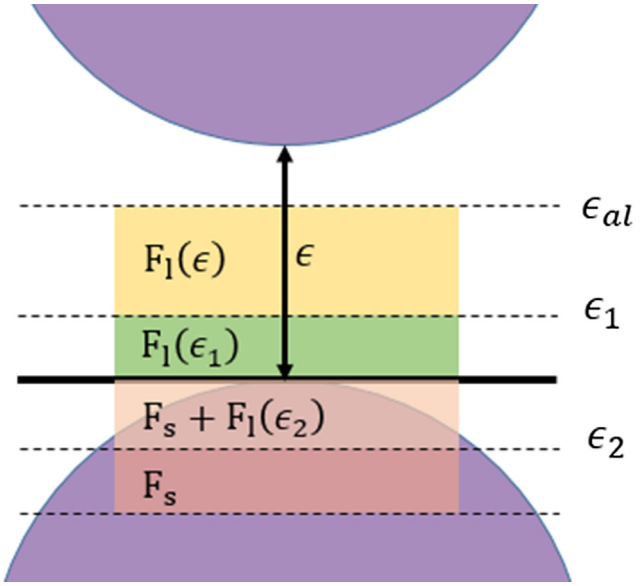

Fig. 2. Multilayer model for hydrodynamic interaction and head-on collision between two spherical particles (Brändle de Motta et al., 2013).

- The van der Waals force model

In the absence of additives such as polymeric flocculants, van der Waals force and electrostatic force are considered to be the dominant forces in colloidal suspensions (Liang et al., 2007). The effect of these forces between particles is commonly simulated using the well-known Derjaguin–Landau–Verwey–Overbeek (DLVO) theory. This theory considers the algebraic summation of van der Waals attractive force and electrical double layer repulsive force. For the simulation of the breakup of aggregates, the electrostatic repulsive force was assumed to be negligible considering chemicals are generally added to neutralize the charges on the surface of particles (Higashitani et al., 2001). Only the van der Waals force is considered for simplicity. The van der Waals interaction, V_{VDW}, is a microscopic-scale force of attraction originating from the permanent and induced electrical interactions between two or more atoms or molecules (Hunter, 2001). For mono-sized particle-particle surface interactions the non-retarded van der Waals potential energy can be evaluated by the Hamaker approximation for short distances. The van der Waals potential V_{VDW} between mono-sized spherical particles i and j, following the model in the work by Zhang and Zhang (2011), is given by the following

$$V_{VDW} = -\frac{A}{6}\left(\frac{2R_1R_2}{r_{ij}^2 - (R_1+R_2)^2} + \frac{2R_1R_2}{r_{ij}^2 - (R_1-R_2)^2} + \ln\left[\frac{r_{ij}^2 - (R_1+R_2)^2}{r_{ij}^2 - (R_1-R_2)^2}\right]\right) \tag{8}$$

where r_{ij} is the distance between the surfaces of two close particles. A is the Hamaker constant, which depends on the geometry and materials of the solid surface, and its value was fixed at 1.5×10^{-20} J (1.51×10^{-20} J in (Peng et al., 2010)). The corresponding interparticle attractive van der Waals force can be derived from $F_{aggr,ij} = -dV_{Aij}/dr_{ij}$ For the given mono-sized particle system, the van der Waals force between two identical spherical particles can be written as:

$$F_{VD}(r) = -\frac{AR_p}{12r^2} \tag{9}$$

A cutoff interaction distance, the same with the particle diameter *dp* beyond which the van der Waals force was negligible, was chosen to minimize the computation. Lubrication force model and the soft-sphere collision model together with the van der Waals force model ensure a good prediction of the particle-particle aggregation process in a homogeneous isotropic turbulence. It is noted that the van der Waals potential tends to infinity as the distance between surfaces of two particles approaches zero. A cut-off distance was defined to overcome this numerical problem and the cut-off distance was taken in accordance with the cut-off distance reported in (Gao et al., 2017).

3. Results and discussion

3.1. Forced particle-laden turbulence

The effects of the introduction of particles into the forced homogeneous isotropic turbulence are studied in this section. Fig. 3 displays the time evolution of volume-averaged whole-field fluctuating velocity and kinetic energy for different concentrations

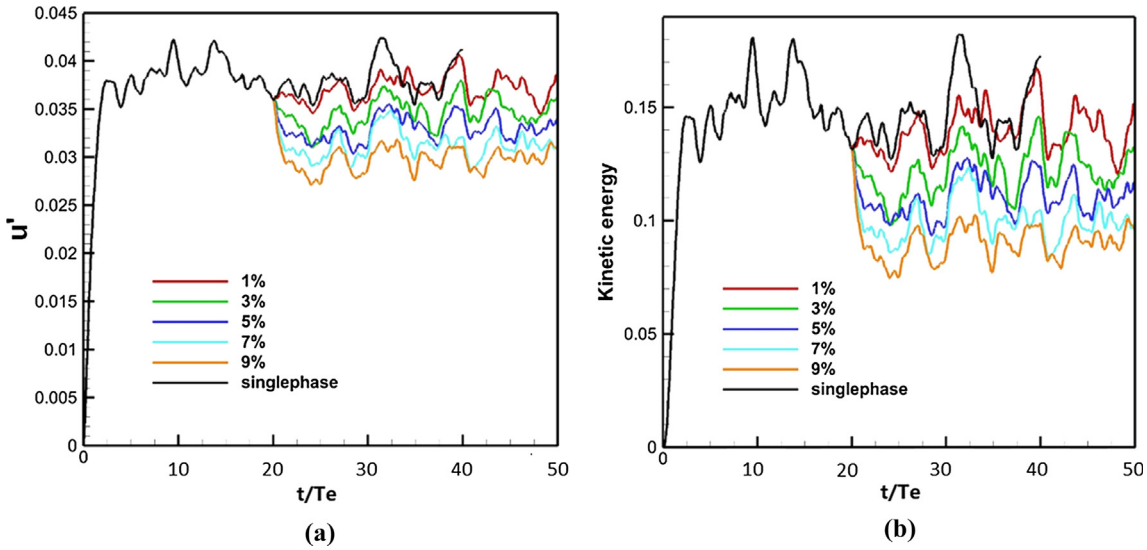

Fig. 3. Evolution of (a) fluctuating velocity and (b) kinetic energy after particles of different particle volume fractions were introduced relative to the single-phase turbulence. The particles were introduced at 20 Te.

of particles. It should be mentioned that the statistical averaging was performed only over the fluid phase. The flow was initially at rest, and the large-scale forcing injected energy into the large scales, which was transferred to smaller scales. Eventually, the viscous dissipation balanced the energy input from the large-scale forcing, and the flow became statistically stationary. Typically, it takes about 3–5 large-eddy turnover times for the flow to reach the stationary stage (Wang et al., 2014b). Particles were introduced at 20 large eddy turnover time. The time evolution of kinetic energy and fluctuating velocity followed the same trend. It was found that the kinetic energy of the system dropped quickly immediately after the introduction of solid particles due to increased viscous dissipation on the particle surfaces. The reduction was more apparent for higher particle concentration. This observation is in accordance with the findings by Abdelsamie and Lee (2012) that the system kinetic energy of particle-laden flow was reduced compared to single-phase turbulence.

Fig. 4 shows the kinetic energy spectra for single phase forced turbulence and particle-laden turbulent flows. When computing the spectra for particle laden flows, the velocity inside a particle is assumed to take the form of a solid body rotation, and as such the full velocity field is properly defined. Compared to the energy spectra of single phase forced turbulence, the energy spectra of particle-laden turbulent flows follow similar trend. It is observed that the energy is attenuated at low wavenumbers where the large-scale forcing is applied, and is augmented at large wavenumbers. This effect has been reported in other studies (Derksen, 2012; Schneiders et al., 2017; Ten Cate et al., 2004; Vreman, 2016; Wang et al., 2014b). Though the forcing field has been only applied to the fluid lattice node, the realized kinetic energy has the proper interpretation of the average kinetic energy of the whole system containing the fluid phase and solid particles. The presence of solid particles increases the resistance to large-scale flow due to the added drag on the solid particles. The disturbance flows around

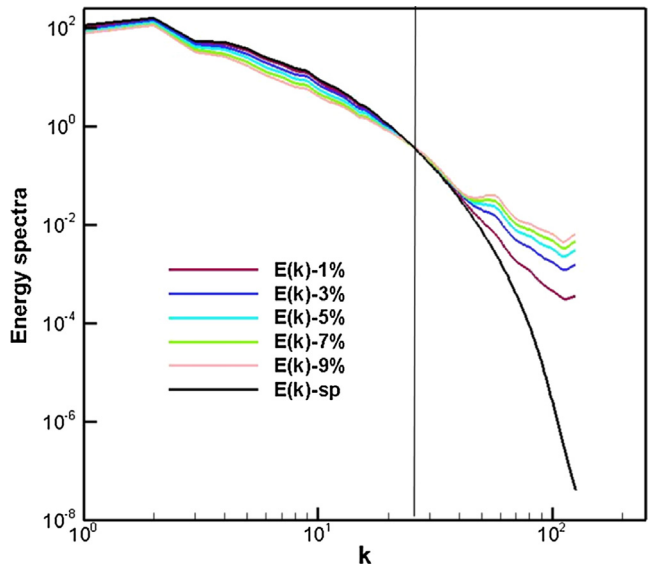

Fig. 4. Kinetic energy spectra for single-phase turbulence and particle-laden aggregating flows with different solid volume fractions. The vertical line marks the crossover point.

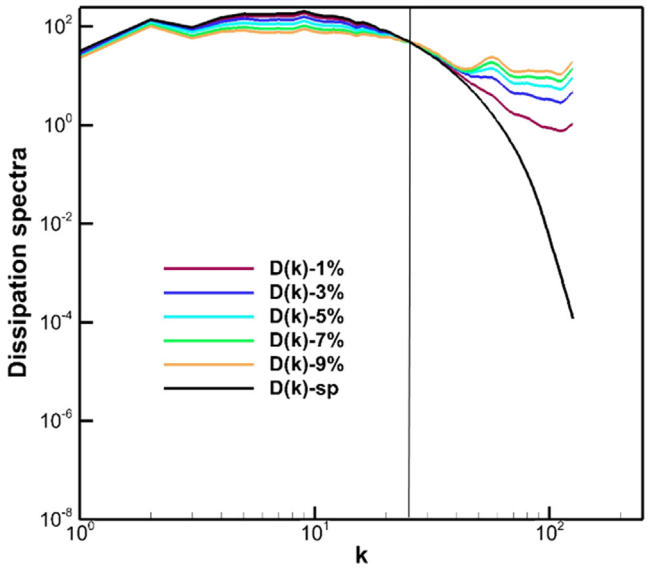

Fig. 5. Dissipation rate spectra for single-phase turbulence and particle-laden aggregating flows with different solid volume fractions. The vertical line marks the crossover point.

the solid particles enhance the high wavenumber energy content, at the cost of reduced low-wavenumber velocity fluctuations.

A similar trend is observed for dissipation rate spectra regarding to energy spectra. Fig. 5 shows the dissipation rate spectra for single phase forced turbulence and particle-laden turbulent flows. The energy dissipation is attenuated at low wavenumbers where the large-scale forcing is applied, and is augmented at large wavenumbers. Flat tails are observed in the dissipation spectrum which was also found in the work by Ten Cate et al. (2004). There will be a discontinuity in the velocity gradient going from the fluid phase into the particle. There are also layers of enhanced vorticity close to the particle surface that are linked to the increased rate of total viscous dissipation. Both of which can give apparently flat tails to the dissipation spectrum. It is interesting to note that the crossover point at which dissipation rate of particle-laden turbulent flows exceed that of the single-phase turbulent flow agrees well with the crossover point in energy spectra plot. Nevertheless, the normalized flow dissipation rates are much larger than the value of the single-phase turbulence and the normalized flow dissipation rates increased with particle volume fractions as is shown in Table 2. This implies that the particle-laden system is much more dissipative than the single-phase turbulence as the enhanced local dissipation at the particle–fluid interfaces leads to enhanced system dissipation.

The volume-averaged statistics averaged over the last 40 eddy turnover times in forced single-phase turbulent flows and particle-laden turbulence are shown in Table 2. Averaging over eddy turnover times provides an approach to estimate the standard deviation of the final averaged value. Let $\sigma_{\bar{A}}$ be the standard deviation of volume-averaged quantity A(t). Eswaran and Pope (1988a) gave a method of calculating the standard deviation of the time-averaged A, and the time-averaged A is

$$\bar{A} = \frac{1}{\Delta T_{ave}} \int_{t_0}^{t_0+\Delta T_{ave}} A(t)dt \tag{10}$$

where ΔT_{ave} is the time duration used for averaging. The standard deviation is

$$\sigma_{\bar{A}} = \sigma_A \sqrt{\frac{2T_c}{\Delta T_{ave}}} \tag{11}$$

where T_c is the correlation time of A(t). In Table 2, we list the statistics for each simulation in the form of mean and standard variance values. The computed flow statistics at the stationary stage, listed in Table 2, include component fluctuation velocity u', the kinetic energy $E(k)$, the flow dissipation rate ϵ, Taylor microscale flow Reynolds number R_λ, resolution parameter $k_{max}\eta$, velocity derivative skewness S, velocity derivative flatness F, the normalized dissipation rate $\epsilon L_f/(u')^3$, Kolmogorov length scale η_K, transverse Taylor microscale λ, longitudinal integral length scale L_f, Kolmogorov velocity v_K, Kolmogorov time τ_K, eddy turnover time T_e. The same flow forcing parameters and fluid properties used for the single phase forced turbulence were adopted for forced turbulence laden with solid particles. We consider the particle–fluid system as a continuous system in local velocity, with velocity inside each particle set to that of solid body rotation. The whole field statistics for five particle-laden LB simulations of different particle volume fractions are plotted in Table 2. Compared to the single phase turbulence, the magnitude of field-averaged dissipation rate and kinetic energy in the particle-laden flow are smaller. The reductions become more apparent with increasing particle volume fraction. Since the dissipation rate is still balanced by the large-scale energy input, this implies that the large-scale energy input is also reduced when compared to the single-phase turbulence. This reduction is partially due to the fact that the forcing was only applied to the region occupied

Table 2
Statistics in forced single-phase turbulent flows and in forced particle-laden turbulence.

variables	Single phase		1%		3%		5%		7%		9%	
	Mean	Standard variance	Mean	Standard variance	Mean	Standard variance	Mean	Standard variance	Mean	Standard variance	Mean	Standard variance
u'	3.82E−02	4.38E−04	3.71E−02	2.41E−04	3.52E−02	2.49E−04	3.32E−02	2.08E−04	3.13E−02	2.32E−04	2.96E−02	2.35E−04
$E(k)$	1.28E + 08	2.97E + 06	1.20E + 08	1.56E + 06	1.08E + 08	1.53E + 06	9.60E + 07	1.21E + 06	8.54E + 07	1.30E + 06	7.67E + 07	1.21E + 06
ϵper unit mass	1.03E + 10	3.01E + 08	1.00E + 10	1.89E + 08	9.84E + 09	1.80E + 08	9.65E + 09	1.45E + 08	9.48E + 09	1.05E + 08	9.72E + 09	1.20E + 08
R_λ	7.50E + 01	1.05E + 00	7.13E + 01	7.07E−01	6.46E + 01	5.74E−01	5.81E + 01	5.83E−01	5.21E + 01	6.47E−01	4.62E + 01	5.46E−01
$k_{max}\eta_K$	2.80E + 00	2.04E−02	2.82E + 00	1.34E−02	2.83E + 00	1.29E−02	2.84E + 00	1.07E−02	2.85E + 00	7.82E−03	2.84E + 00	8.63E−03
Skewness$S$	−4.95E−01	1.94E−03	−4.54E−01	1.57E−03	−3.28E−01	1.98E−03	−2.08E−01	1.88E−03	−1.17E−01	1.56E−03	−5.87E−02	9.38E−04
Flatness$F$	4.83E + 00	2.54E−02	7.53E + 00	3.02E−02	1.41E + 01	1.76E−01	1.95E + 01	2.46E−01	2.33E + 01	9.16E−02	2.46E + 01	1.74E−01
$\epsilon L_f/(u')^3$	5.70E−01	7.38E−03	6.08E−01	6.81E−03	7.11E−01	6.58E−03	8.43E−01	6.32E−03	1.02E + 00	8.70E−03	1.25E + 00	1.25E−02
η_K	9.03E−01	6.56E−03	9.08E−01	4.30E−03	9.12E−01	4.16E−03	9.15E−01	3.44E−03	9.19E−01	2.52E−03	9.13E−01	2.78E−03
λ	1.54E + 01	1.44E−01	1.51E + 01	1.08E−01	1.44E + 01	8.21E−02	1.37E + 01	8.69E−02	1.30E + 01	7.58E−02	1.22E + 01	6.42E−02
L_f	4.36E + 01	4.77E−01	4.34E + 01	4.81E−01	4.40E + 01	3.89E−01	4.47E + 01	5.87E−01	4.60E + 01	5.99E−01	4.69E + 01	5.25E−01
v_K	8.70E−03	6.34E−05	8.65E−03	4.09E−05	8.61E−03	3.93E−05	8.57E−03	3.22E−05	8.54E−03	2.35E−05	8.59E−03	2.63E−05
τ_K	1.04E + 02	1.51E + 00	1.05E + 02	9.98E−01	1.06E + 02	9.65E−01	1.07E + 02	8.05E−01	1.08E + 02	5.89E−01	1.06E + 02	6.46E−01
T_e	2.02E + 03	3.90E + 01	1.94E + 03	2.77E + 01	1.77E + 03	2.02E + 01	1.60E + 03	2.05E + 01	1.45E + 03	1.71E + 01	1.27E + 03	1.34E + 01

by the fluid. It should be mentioned that higher order moments of the velocity derivative may be inaccurate and higher grid resolution is needed to accurately resolve the local dissipation rate at the particle surface. We used the same background turbulence as in Wang et al. (2014b). Grid refinement has been performed in Wang et al. (2014a,b)'s tests and grid resolution of 256 points in each direction was compared to 512 points. When 16 lattice units instead of 8 lattice units was used for one particle diameter, the overall turbulent statistics did not change much as is shown in the table from Wang et al. (2014a,b), meaning that 8 lattice units was sufficient for one particle diameter. In that case, a grid resolution of 256 points in each direction appeared to be sufficient for most turbulent statistics, except the velocity flatness. However, the rather high horizontal tails of the dissipation spectra in some of the present cases (Fig. 5) suggest that, in these cases, the dissipation rate and other statistics of velocity derivatives are only marginally resolved.

3.2. Aggregation in forced homogeneous isotropic turbulence

Aggregation of particles in homogeneous isotropic turbulence is dependent not only on the self-interactions between aggregates, but also the turbulence which requires an appropriate domain size. The cubic domain should be much larger than the aggregate size to achieve representative results for the purpose of avoiding unphysical situation that an aggregate strongly interacts with itself through the periodic boundary (Derksen, 2012). The Kolmogorov length scale over particle diameter is 0.11. A representation of particle aggregation with solid volume concentration at 5% is given in Fig. 6. Fig. 6A shows the initial distribution of particles in the cubic, which is evenly distributed. After 30 large eddy turnover time, a snapshot of particle configurations is given in Fig. 6B. It appears that large aggregate structures comparable to the size of cubic are formed. This is due to the appearance that aggregates in front block the view of aggregates in the back. To show the largest aggregate formed in this case, we extracted two largest aggregates as is shown in Fig. 6C. The size of domain is much larger than the size of the largest aggregate. Derksen (2012) considered that aggregate size distribution was fairly independent of the size of the flow domain when the length of domain was 16 times higher than the diameter of primary particles. In our studies, the length of domain to the diameter of primary particles were always kept at 32. Therefore, the periodic flow domain is sufficiently large to develop a dynamically stationary aggregate size distribution.

To study statistically the contacts between particles, time series of particle-particle contacts are plotted in Fig. 7. A striking observation is that the aggregating systems can quickly get unstable and the number of contacts between particles increases sharply in the first two large eddy turnover time after the introduction of particles. The number of contacts remain at certain level after four times of eddy turnover time. This means that the system quickly reaches a dynamically stationary state with continuous attachment and detachment of particles. It should be pointed out that simulations were carried out for different particle concentration ranging from 1 to 9% under same turbulence intensity. The number of contacts increase with the particle concentration.

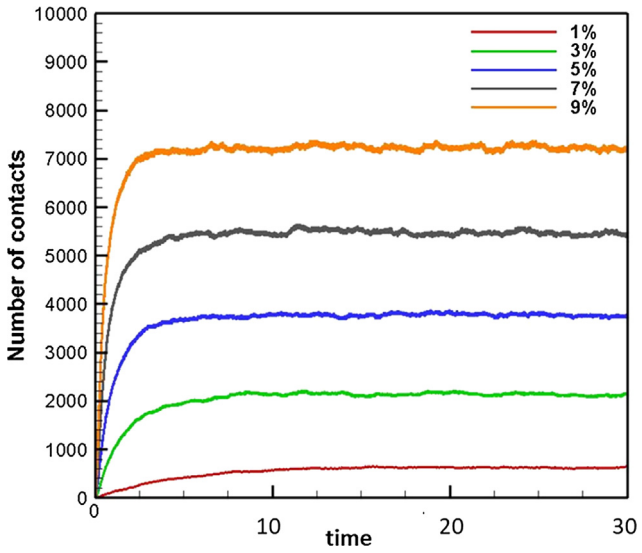

Fig. 7. Time series of the number of contacts in aggregation system consisted of different particle volume fractions.

To illustrate the relationship between the number of contacts and the particle volume fractions, we plot the number of contacts as a function of particle volume fraction as is shown in Fig. 8. A clear linear relationship is found between the number of contacts and the particle volume fraction representing the number of particles. The aggregates presented in this article are by aggregate volume (which is the same as by aggregate mass or by aggregate size in terms of the number of primary spheres). This is intuitively logical that the number of contacts between particles in the turbulence increases with the number of particles. Nevertheless, number of contacts is generally believed to be dependent on the number of particle pairs, which is a function of square of particle number. It should be pointed out that this theory is true for particle-laden turbulent flows with particles that are freely moving. Our simulations are different scenario that particles are aggregating and may stick to other particles in the turbulent flows. This may result in the linear relationship between the number of contacts and the number of particles.

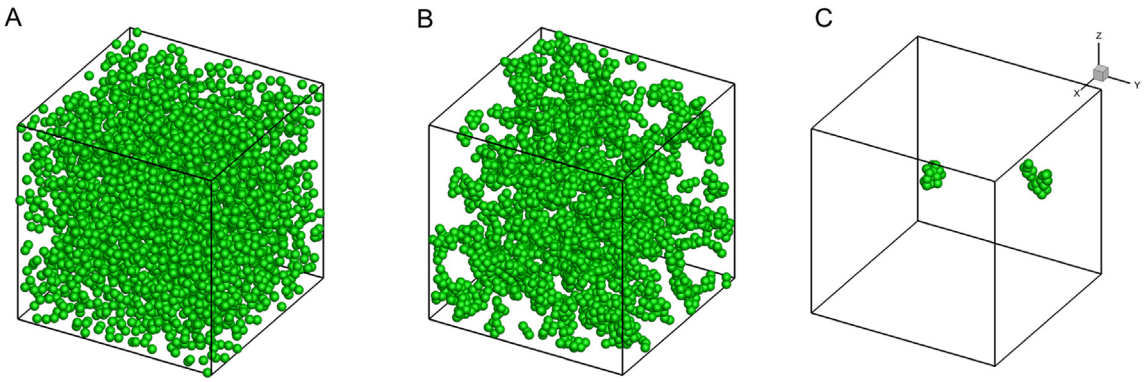

Fig. 6. Single realization of aggregation with particle concentration at 5%: A, initial state of particle distribution; B, a snapshot of particle aggregating at 30Te after the introduction of particles; C, two largest aggregates taken from Figure B.

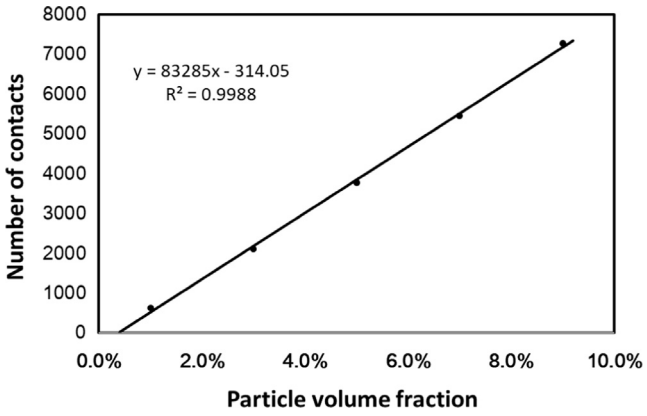

Fig. 8. Number of contacts as a function of particle volume fraction.

To make the observations regarding the aggregation process more quantitative, time-averaged aggregate size distributions for five different solid concentrations were determined. The aggregation system is unstable after the introduction of particles. Therefore, we analyze the statistics of aggregates after 10 large eddy turnover time and the aggregation system reaches dynamic stationary state. Since the aggregate size distribution is obtained during a stationary time window, turbulence is maintained at same level for different particle concentrations. A large number of instantaneous realizations for 20 large eddy turnover time have been analyzed and Fig. 9 shows aggregate size distributions for five different solid concentrations under the same turbulent flows. Aggregates size distributions follow similar trends for different particle volume fraction. Most of particles are in the small aggregate size region and this is in accordance with the observations in Derksen (2012). The effects of particle volume fraction on the aggregate size distribution can be observed in a way that a shift toward larger aggregate sizes appears if the particle volume fraction is increased. The scenario that large aggregates formed in dense suspension is due to the reason that collisions are much more frequent, whilst, smaller aggregates develops in more dilute suspensions because collisions are much less frequent in the dilute suspensions.

Aggregation of particles can be characterized by the particle radial distribution function (RDF) $g(r_i)$, which is defined as

$$g(r_i) = \frac{N_i/V_i}{N/V} \tag{12}$$

where Ni is the number of particle pairs separated with a distance $(ri - \Delta r, ri + \Delta r)$, Vi is the shell volume of $4\pi[(ri + \Delta r)^3 - (ri - \Delta r)^3]$ /3, N is the total number of particle pairs Np $(Np - 1)/2$ and V is the total volume $LxLyLz$. ri is the radial distance between two particle centers. The radial distribution functions for the same cases in Fig. 9 are calculated and presented in Fig. 10. Similar trend is observed for different particle volume fractions as in the plot of aggregate size distribution. Peaks appeared around $2R_p$ for different particle volume fractions, and this means that most of aggregates were consisted of two primary particles. A shift towards larger aggregate sizes is observed if the particle volume fraction is increased. A dynamic study of aggregation is presented in Fig. 11, where radial distribution functions for particle volume fraction of 9% at different time states are given. t0 is the time when particles are first introduced into the homogeneous isotropic turbulence. In this case, the PDF is zero at $ri = R_p$ and is flat after reaching climax. This means that particles are evenly distributed across the volume and no particles overlap initially, as designed in the simulations. The aggregating system is highly unstable, and the radial distribution function changes significantly over first two large eddy turnover time. An apparent peak is formed at $ri = R_p$ as is observed in Fig. 10. The peak grows with time and becomes stable when the aggregating system reaches a dynamic stationary state, meaning that particles attach and detach constantly reaching an equilibrium state. It should be pointed out that the particle preferential concentration due to inertia drives particles together that increases their chance to collide and aggregate. This accumulation effect combined with the attractions between particles make aggregations more apparent in dense suspensions.

The flow field with the particles aggregate is shown in Fig. 12. Fig. 12a is a snapshot of fluid velocity distribution on a slice at z = 128.5 for particle volume fraction of 9% when the particles are first introduced. Fig. 12b shows the visualization on the same slice after 30 times large eddy turnover time. Particles are initially evenly distributed and a large number of aggregates are formed after aggregation finishes. It is clear that regions of high velocity appear to be more structured in the slice where aggregation has finished when compared to that in the slice when particles are first introduced. Due to the effect of surrounding flow field around the

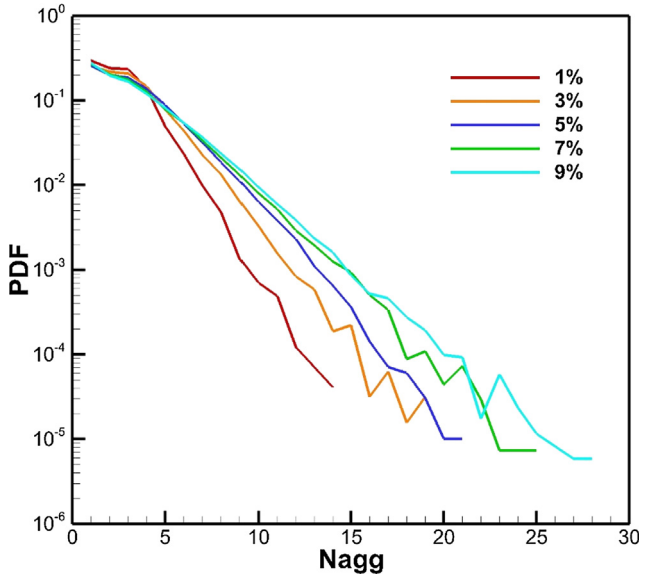

Fig. 9. Aggregate size (the number of primary particles) distribution for different particle volume fractions.

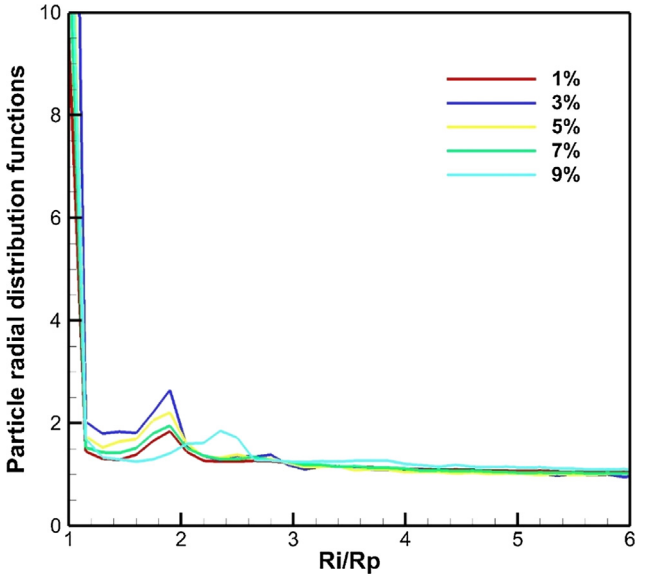

Fig. 10. The particle radial distribution functions for different particle volume fractions in the particle-laden forced turbulent flow simulations.

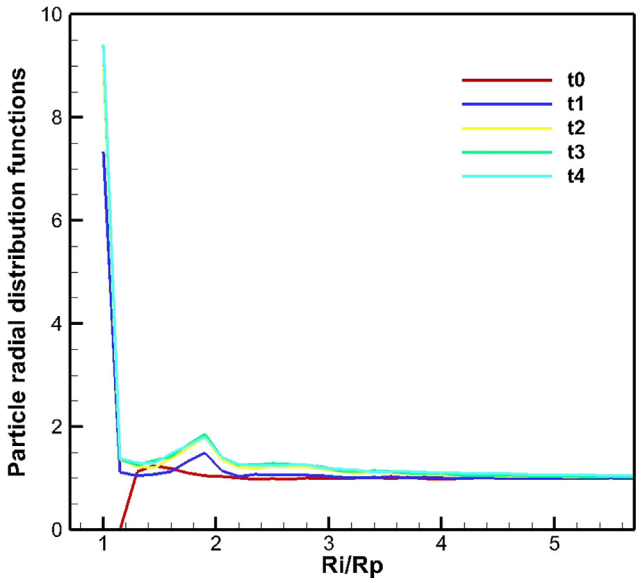

Fig. 11. The particle radial distribution functions for 9% fractions in the particle-laden forced turbulent flow simulations at different times: $t_0 = 0$, $t_1 = Te$, $t_2 = 2Te$, $t_3 = 3Te$, $t_4 = 4Te$.

aggregating particles, particles are pushed together and large aggregates are formed. The fluid velocity magnitude is less near the particle surface, as expected from the no-slip condition and the lower particle velocity fluctuations. The damping effect on the surrounding flow field is the essence of two-way interactions between liquid flow and aggregating particles. Particles are pushed together and aggregate, which leads to more significant damping effect on the turbulent liquid flow. It is observed that large aggregates are typically nearby regions of low shear rate. This can be explained as large aggregates are sheared into pieces by high liquid velocity shear and reformulate in the region of low shear rate.

Fig. 13 shows the contours of fluid vorticity magnitude corresponding to the same flows as is shown in Fig. 12. It is clear that there are patches of high vorticity near the surfaces of solid particles in the aggregated system due to the viscous boundary layers. Fig. 13a shows the size of the smaller flow structures is comparable to the size of the primary particles. Van Vliet et al. (2005) suggest that the smallest scales that show up have a size of the order of $10\eta_K$ in the flow visualized in a similar way as in Fig. 13. The scale is comparable to the size of the primary particles. Due to the existence of large particle aggregates, the turbulent flow is smoothed out. Vortex shedding is observed in the wake associated with particle aggregates in the slice shown in Fig. 13b. It could be possible that the turbulent background field might induce vortex-shedding at much lower particle Reynolds number and the local particle Reynolds number could be significantly higher (Derksen, 2012). Visualization of vorticity magnitude shows that patches of high vorticity tend to be found near the particle surfaces.

3.3. Discussion

Aggregation of particles is a physic-chemical process where chemical environment should be tuned for it to occur. The chemistry in the suspension composed of colloidal particles determines the interactions between particles as either repulsive or attractive, which is vital for aggregation. When particles are repulsive towards each other, the suspension is stable though turbulence is applied to induce aggregation. We consider the chemistry has been well taken care of in our simulation and in this way the interactions between particles can be accounted by simply considering the van der Walls force and lubrication force accompanied with soft-sphere collision force. Hydrodynamics in the suspension is another important parameter in describing particle aggregation. High-intensity turbulence facilitates the aggregation of particles by bringing particles together. On the other hand high-intensity turbulence also causes attached particles to detach from aggregation. The balance of the two determines the preferred or maximum aggregate size. Therefore, turbulence is favorable in the first stage to destabilize colloidal particle suspension system, whilst, turbulence is unfavorable for aggregates to grow. In the water treatment industry, high turbulence is generally applied to induce aggregation by giving particles sufficient kinetic energy to overcome barriers (Rubio et al., 2002). This generally occur in rapid mixing process, after which low turbulence is applied to the suspension for aggregates to grow and finally settle in the bottom of the tank. Turbulence in the suspension should be modulated for specific purposes. Most of CFD studies of aggregation considered the size of particles smaller than Kolmogorov scale and particles were therefore considered as point particles. In this way, the effects of

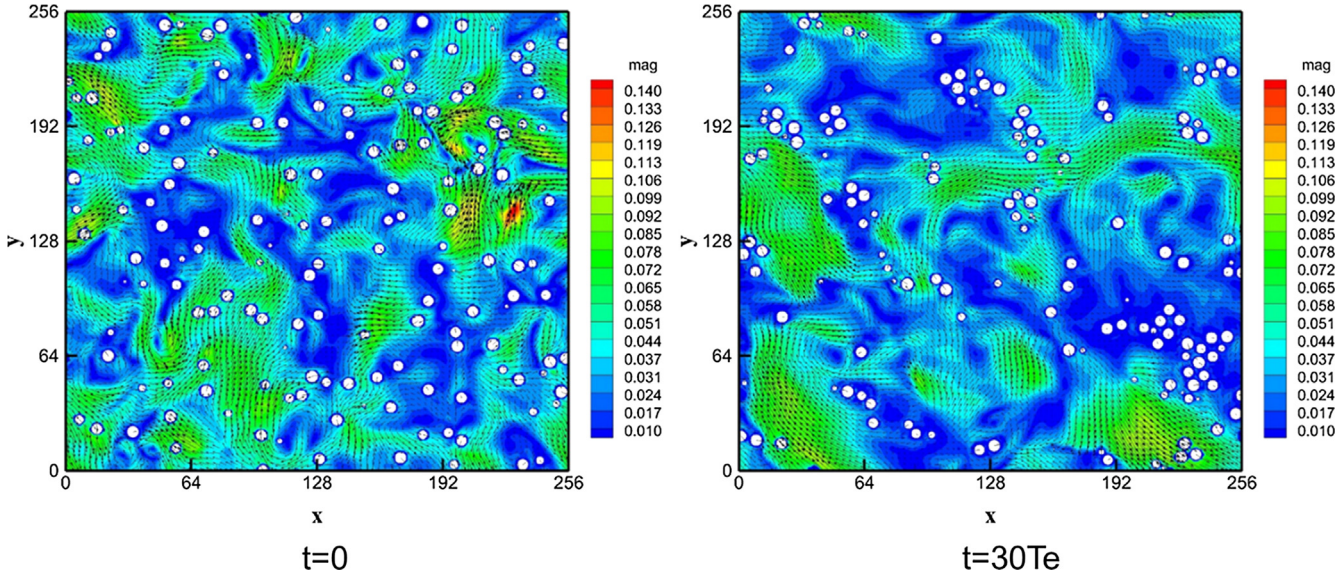

Fig. 12. Contours of fluid velocity magnitude and particle position in an x-y plane z = 128.5 superimposed with velocity vectors, at the start of simulation with particle evenly inserted and at the end of simulation when t equals 30 times eddy turnover time.

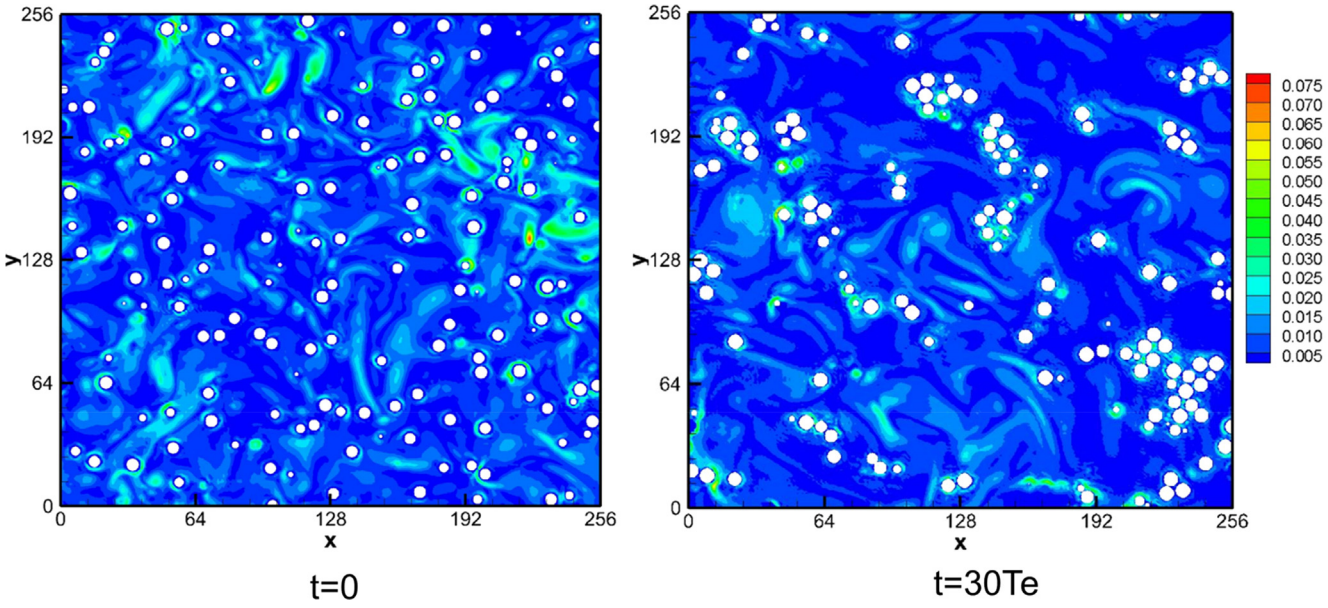

Fig. 13. Contours of fluid vorticity magnitude and particle position in an x-y plane z = 128.5 at the start of simulation with particle evenly inserted and at the end of simulation when t equals 30 times eddy turnover time.

flow on the aggregation process is considered but not the other way around. This is appropriate when microscales in the turbulent suspension is larger than the aggregates and this separation is wide. However, this assumption does not hold for cases where high energy input exists and the size of aggregates are comparable to the size of turbulent microscales. A good example is represented by the downcomer in Jameson cell which is used for wastewater treatment (Jameson, 2010). A high-speed jet is used to generate a turbulent flow of high intensity, where microscale structures are believed to be in the scale comparable to the size of particles.

We considered the size of particle larger than Kolmogorov scales and phase interactions between turbulent flow and aggregating particles were fully coupled. Though the system we studied was relatively simple in a way that single-sized spherical particles aggregated in a homogeneous isotropic turbulence and the flow domain was periodic in all directions, the flow around the aggregating particles was resolved. Therefore, we were able to explicitly simulate the effects of the interacting length scales (particle and aggregate size), which is key as turbulent structures in the scale comparable to the sizes of aggregates are considered most influential to the aggregation process (Derksen, 2012). The interactions between turbulence and the aggregation process was studied from two perspectives: the effects of aggregating particles on turbulence and particles aggregating in forced turbulence. Particles were observed to aggregate rapidly due to the promoted collisions by turbulence. Aggregation then entered into a dynamic stationary stage that particles attached and detached constantly reaching a dynamic equilibrium state. This is determined by the counterbalance between turbulence shear induced breaking and particle aggregation. It is clear that turbulence in the suspension cannot be maintained at high level for further growth of particle aggregates as local shear flow from turbulence can lead to breakage of aggregates. After the suspension system is destabilized by turbulence of high intensity, low turbulence is preferred for aggregates to grow further.

4. Conclusion

The LBM computational technique incorporated with the van der Waals force model was successfully applied to gain a better insight into the aggregation behaviour of a mono-sized spherical particle system in a homogeneous and isotropic turbulence. The aggregation simulations were conducted under the same reproducible hydrodynamic conditions. This approach allows aggregation to be studied for different particle volume fractions under the same controlled turbulent flow environment. The modulation of turbulence by aggregating particles of different volume fractions and phase interactions between aggregating particles and turbulent flows during aggregation have been studied. The existence of particles was found to have profound impact on turbulent flows. Energy and dissipation spectra was attenuated at low wavenumbers where the large-scale forcing was applied, and was augmented at large wavenumbers. The effect of solid volume fraction on the aggregate growth was also studied. It was found that aggregates size distributions and radial distribution functions followed similar trends for different particle volume fractions. The overall influence of the solid volume fractions on aggregate size distribution was found to be negligible over the examined range of conditions. However, it was evident that a shift toward larger aggregate sizes appeared if the particle volume fraction was increased for the reason that collisions were much more frequent in dense suspensions. A clear linear relationship was found between the number of contacts and the particle volume fraction representing the number of particles. A rapid aggregation was observed for solid volume fractions in the examined range under the studied turbulence conditions, after which the aggregating system quickly reached a dynamically stationary state with continuous attachment and detachment of particles.

Conflict of interest

The authors declared that there is no conflict of interest.

Acknowledgement

We gratefully acknowledge that this work was supported by Grand Research Project of National Natural Science Foundation of China“91852205”.

Appendix A. Supplementary material

Supplementary data to this article can be found online at https://doi.org/10.1016/j.ces.2019.03.004.

References

Abdelsamie, A.H., Lee, C., 2012. Decaying versus stationary turbulence in particle-laden isotropic turbulence: turbulence modulation mechanism. Phys. Fluids 24, 015106.

Babler, M.U., Biferale, L., Brandt, L., Feudel, U., Guseva, K., Lanotte, A.S., Marchioli, C., Picano, F., Sardina, G., Soldati, A., 2015. Numerical simulations of aggregate breakup in bounded and unbounded turbulent flows. J. Fluid Mech. 766, 104–128.

Babler, M.U., Biferale, L., Lanotte, A.S., 2012. Breakup of small aggregates driven by turbulent hydrodynamical stress. Phys. Rev. E 85, 025301.

Brändle de Motta, J., Breugem, W.-P., Gazanion, B., Estivalezes, J.-L., Vincent, S., Climent, E., 2013. Numerical modelling of finite-size particle collisions in a viscous fluid. Phys. Fluids 25, 083302.

Bratby, J., 2006. Coagulation and Flocculation in Water and Wastewater Treatment. IWA publishing.

Bridgeman, J., Jefferson, B., Parsons, S.A., 2009. Computational fluid dynamics modelling of flocculation in water treatment: a review. Eng. Appl. Comput. Fluid Mech. 3, 220–241.

Chen, S., Doolen, G.D., 1998. Lattice Boltzmann method for fluid flows. Annu. Rev. Fluid Mech. 30, 329–364.

Chouippe, A., Uhlmann, M., 2015. Forcing homogeneous turbulence in direct numerical simulation of particulate flow with interface resolution and gravity. Phys. Fluids 27, 123301.

Derksen, J., 2012. Direct numerical simulations of aggregation of monosized spherical particles in homogeneous isotropic turbulence. AIChE J. 58, 2589–2600.

Ernst, M., Dietzel, M., Sommerfeld, M., 2013. A lattice Boltzmann method for simulating transport and agglomeration of resolved particles. Acta Mech. 224, 2425–2449.

Eswaran, V., Pope, S., 1988a. An examination of forcing in direct numerical simulations of turbulence. Comput. Fluids 16, 257–278.

Eswaran, V., Pope, S.B., 1988b. An examination of forcing in direct numerical simulations of turbulence. Comput. Fluids 16, 257–278.

Gao, H., Li, H., Wang, L.-P., 2013. Lattice Boltzmann simulation of turbulent flow laden with finite-size particles. Comput. Math. Appl. 65, 194–210.

Gao, Y., Evans, G.M., Wanless, E.J., Moreno-Atanasio, R., 2017. DEM modelling of particle-bubble capture through extended DLVO theory. Colloids Surf. A 529, 876–885.

Higashitani, K., Iimura, K., Sanda, H., 2001. Simulation of deformation and breakup of large aggregates in flows of viscous fluids. Chem. Eng. Sci. 56, 2927–2938.

Hunter, R.J., 2001. Foundations of Colloid Science. Oxford University Press.

Jameson, G.J., 2010. New directions in flotation machine design. Miner. Eng. 23, 835–841.

Karpinska, A.M., Bridgeman, J., 2016. CFD-aided modelling of activated sludge systems–A critical review. Water Res. 88, 861–879.

Kromkamp, J., van den Ende, D., Kandhai, D., van der Sman, R., Boom, R., 2006. Lattice Boltzmann simulation of 2D and 3D non-Brownian suspensions in Couette flow. Chem. Eng. Sci. 61, 858–873.

Ladd, A., Verberg, R., 2001. Lattice-Boltzmann simulations of particle-fluid suspensions. J. Stat. Phys. 104, 1191–1251.

Ladd, A.J., 1994a. Numerical simulations of particulate suspensions via a discretized Boltzmann equation. Part 1. Theoretical foundation. J. Fluid Mech. 271, 285–309.

Ladd, A.J., 1994b. Numerical simulations of particulate suspensions via a discretized Boltzmann equation. Part 2. Numerical results. J. Fluid Mech. 271, 311–339.

Lallemand, P., Luo, L.-S., 2003. Lattice Boltzmann method for moving boundaries. J. Comput. Phys. 184, 406–421.

Liang, Y., Hilal, N., Langston, P., Starov, V., 2007. Interaction forces between colloidal particles in liquid: theory and experiment. Adv. Colloid Interface Sci. 134, 151–166.

Nguyen, N.-Q., Ladd, A., 2002. Lubrication corrections for lattice-Boltzmann simulations of particle suspensions. Phys. Rev. E 66, 046708.

Nguyen, N.-Q., Ladd, A.J., 2005. Sedimentation of hard-sphere suspensions at low Reynolds number. J. Fluid Mech. 525, 73–104.

Peng, Z., Doroodchi, E., Evans, G., 2010. DEM simulation of aggregation of suspended nanoparticles. Powder Technol. 204, 91–102.

Peng, Z., Doroodchi, E., Evans, G.M., 2012a. Influence of primary particle size distribution on nanoparticles aggregation and suspension yield stress: a theoretical study. Powder Technol. 223, 3–11.

Peng, Z.B., Doroodchi, E., Moghtaderi, B., Evans, G.M., 2012b. A DEM-based analysis of the influence of aggregate structure on suspension shear yield stress. Adv. Powder Technol. 23, 437–444.

Rubio, J., Souza, M.L., Smith, R.W., 2002. Overview of flotation as a wastewater treatment technique. Miner. Eng. 15, 139–155.

Saha, D., Babler, M.U., Holzner, M., Soos, M., Lüthi, B., Liberzon, A., Kinzelbach, W., 2015. Breakup of finite-size colloidal aggregates in turbulent flow investigated by three-dimensional (3D) particle tracking velocimetry. Langmuir 32, 55–65.

Samaras, K., Zouboulis, A., Karapantsios, T., Kostoglou, M., 2010. A CFD-based simulation study of a large scale flocculation tank for potable water treatment. Chem. Eng. J. 162, 208–216.

Schneiders, L., Meinke, M., Schröder, W., 2017. Direct particle–fluid simulation of Kolmogorov-length-scale size particles in decaying isotropic turbulence. J. Fluid Mech. 819, 188–227.

Sun, R., Xiao, H., Sun, H., 2018. Investigating the settling dynamics of cohesive silt particles with particle-resolving simulations. Adv. Water Resour. 111, 406–422.

Ten Cate, A., Derksen, J.J., Portela, L.M., Van Den Akker, H.E., 2004. Fully resolved simulations of colliding monodisperse spheres in forced isotropic turbulence. J. Fluid Mech. 519, 233–271.

Thomas, D.N., Judd, S.J., Fawcett, N., 1999. Flocculation modelling: a review. Water Res. 33, 1579–1592.

Vadasarukkai, Y.S., Gagnon, G.A., Campbell, D.R., Clark, S.C., 2011. Assessment of hydraulic flocculation processes using CFD. Am. Water Works Associat. J. 103, 66.

Van Vliet, E., Derksen, J., Van den Akker, H., 2005. Turbulent mixing in a tubular reactor: assessment of an FDF/LES approach. AIChE J. 51, 725–739.

Vandamme, D., Foubert, I., Muylaert, K., 2013. Flocculation as a low-cost method for harvesting microalgae for bulk biomass production. Trends Biotechnol. 31, 233–239.

Vreman, A., 2016. Particle-resolved direct numerical simulation of homogeneous isotropic turbulence modified by small fixed spheres. J. Fluid Mech. 796, 40–85.

Wang, C., Harbottle, D., Liu, Q., Xu, Z., 2014a. Current state of fine mineral tailings treatment: a critical review on theory and practice. Miner. Eng. 58, 113–131.

Wang, G., Bai, X., Wu, C., Li, W., Liu, K., Kiani, A., 2018a. Recent advances in the beneficiation of ultrafine coal particles. Fuel Process. Technol. 178, 104–125.

Wang, G.C., Ge, L.H., Mitra, S., Evans, G.M., Joshi, J.B., Chen, S.Y., 2018b. A review of CFD modelling studies on the flotation process. Miner. Eng. 127, 153–177.

Wang, L.-P., Ayala, O., Gao, H., Andersen, C., Mathews, K.L., 2014b. Study of forced turbulence and its modulation by finite-size solid particles using the lattice Boltzmann approach. Comput. Math. Appl. 67, 363–380.

Zhang, J.-F., Zhang, Q.-H., 2011. Lattice Boltzmann simulation of the flocculation process of cohesive sediment due to differential settling. Cont. Shelf Res. 31, S94–S105.

Zhang, J.-F., Zhang, Q.-H., Maa, J.P.-Y., Qiao, G.-Q., 2013. Lattice Boltzmann simulation of turbulence-induced flocculation of cohesive sediment. Ocean Dyn. 63, 1123–1135.

Zhang, Q.-H., Zhang, J.-F., 2008. Modeling of 3D fractal mud flocs settling via lattice Boltzmann method. In: Proceedings in Marine Science. Elsevier, pp. 227–240.

Zhou, K., Hou, J., Sun, Q., Guo, L., Bing, S., Du, Q., Yao, C., 2017. An efficient LBM-DEM simulation method for suspensions of deformable preformed particle gels. Chem. Eng. Sci. 167, 288–296.